

MULTISCALE EXPERIMENTS AND MODELING IN BIOMATERIALS AND BIOLOGICAL MATERIALS

Design of Functionalized Lobed Particles for Porous Self-Assemblies

BISWAJIT GORAI $^{\odot}$, BRUNNO C. ROCHA $^{\odot}$, and HARISH VASHISTH $^{\odot}$ 1,2

1.—Department of Chemical Engineering, University of New Hampshire, Durham 03824, NH, USA. 2.—e-mail: harish.vashisth@unh.edu

Colloidal particles fabricated with anisotropic interactions have emerged as building blocks for designing materials with various nanotechnological applications. We used coarse-grained Langevin dynamics simulations to probe the morphologies of self-assembled structures formed by lobed particles decorated with functional groups. We tuned the interactions between the functional groups to investigate their effect on the porosity of self-assembled structures formed by lobed particles with different shapes (snowman, dumbbell, trigonal planar, tetrahedral, square planar, trigonal bipyramidal, and octahedral) at different temperatures. The dumbbell, trigonal planar, and square planar shaped particles, with planar geometries, form self-assembled structures including elongated chains, honeycomb sheets, and square sheets, respectively. The particles with non-planar geometries (tetrahedral, trigonal bipyramidal, and octahedral) self-assemble into random aggregate morphologies. The structures formed by trigonal bipyramidal and octahedral particles exhibit smaller and homogeneous pores compared to the structures formed by trigonal planar and square planar particles. The porosity in selfassembled structures is substantially enhanced by the functionalization of

particles.
Nomenclature
Potential of hydrogen
Gold nanoparticle
Deoxyribonucleic acid
Molecular dynamics
Monte Carlo
Boltzmann constant
Depth of the potential well in the Lennard-
Jones potential equation
Diameter of the particle
Mass of the particle
Temperature
$k_{ m B}{ m T}/\epsilon$
Seed
Lobe
Functional group
Number of functional groups
Snowman particle
Dumbbell particle
Trigonal planar particle
Tetrahedral particle
Square planar particle

Octahedral particle $\vec{k_{bond}}$ Force constant for bonds $k_{angle} \ ext{SSLJ}$ Force constant for angles Surface shifted Lennard-Jones potential Distance between particles i and j r_{ii} Cut-off distance r_{cut} RDF Radial distribution function Density Pair correlation function g(r)PSD Pore size distribution D_{LFS} Diameter of the largest free sphere $\langle E_p \rangle$ Average potential energy per particle

INTRODUCTION

Colloids with anisotropic interactions are the nanoscopic building blocks for self-assembly into complex structures with distinct morphologies. The bottom-up technique of colloidal self-assembly facilitates the formation of well-defined superstructures by controllable and site-specific interactions. The efforts to design building blocks with anisotropic properties have seen a transition

(Received February 20, 2021; accepted April 26, 2021)

Trigonal bipyramidal particle

Published online: 01 June 2021

in the architecture of spherical patchy particles from two-faced Janus colloids to multiblock colloidal particles. ¹⁷ Moreover, non-spherical customized colloids of different shapes with single or multiple protrusions have been achieved using multi-step swelling and emulsification techniques to further enhance the anisotropic dimensionality and procure particle assemblies with specific features. ^{18–21}

Colloidal particles have also found utility in designing hydrogels that are cross-linked polymeric materials with applications in drug-delivery systems, biomolecular sensors, tissue engineering, and scaffolds for cell growth. The poly(vinyl alcohol) hydrogels are biocompatible and possess stable mechanical characteristics at a broad range of temperatures and pH.^{22–25} Rossi et al.²⁶ synthesized polymeric hydrogels functionalized with biodegradable nanoparticles to achieve a hydrogel matrix useful for controlled drug delivery. Moreover, the non-toxic β -peptide hydrogels self-assembled in aqueous solvent to form a mechanically stable and biocompatible matrix with enhanced self-healing property.²⁷ The hydrogels are functionally tailored using proteins, nucleotides, polymers, nanoparticles, and chemical scaffolds to facilitate the formation of extracellular matrix for biological applications. 28-32 The swelling/deswelling during dispersion and emulsion polymerization-based techniques are tuned by various external stimuli to synthesize hydrogel colloids.33 For example, the poly(N-isopropylacrylamide)-based microgel colloids are functionalized with different groups to develop characteristic features for versatile applications.³⁴

Furthermore, a library of colloidal patchy molecules with modified properties has been obtained by attaching functional moieties with specific physicochemical properties. The patches on colloidal particles have also been site-specifically decorated by oligonucleotides with sticky ends to obtain diverse self-assembled morphologies.³⁵ Klinkova et al.³ have achieved the linear aggregation of gold nanorods functionalized with polystyrene at both ends. Schreiber et al.³⁷ controlled the self-assembly of gold nanoparticles (AuNPs) functionalized with cross-linked DNA helices by precisely varying the position of complementary linker oligonucleotides. They obtained long chains and square and hexagonal lattices of AuNPs after varying the position and stoichiometry of the complementary linker oligonucleotides.

Inspired by these experimental studies, the self-assembly of simplified models of hydrogels and functionalized colloidal patchy particles has been studied using molecular dynamics (MD) simulations. For example, the damage and recovery of hybrid cross-linked hydrogel models were investigated using MD simulations.³⁸ In another simulation study,³⁹ the degree of crosslinking of polymer chains, with some magnetic beads, was investigated. This study showed the size of microgels contracts after increasing the concentration of

magnetic beads. Adroher-Benítez et al.⁴⁰ performed coarse-grained Monte Carlo (MC) simulations and showed that the swelling and the charge distributions inside thermo-responsive charged nanogels can be controlled by the local concentration of counterions in the media. Also, the self-assembly of amphiphilic colloids (Janus particles), lobed patchy particles, and spherical colloids have been investigated in detail using computer simulations. ^{3,41–47} However, the self-assembly of hydrogel type colloidal lobed particles decorated with different functional groups has not been probed systematically yet.

In our earlier work, 48,49 we introduced models of different types of non-spherical hard-lobed patchy particles and investigated their self-assembly using coarse-grained MD simulations. We obtained distinct self-assembled amorphous as well as crystalline porous morphologies for all types of particles, except the snowman shaped particles with a single lobe. The tetrahedral, trigonal bipyramidal, and octahedral shaped particles self-assembled into compact porous crystalline structures, and the linear dumbbell, trigonal planar, and square planar shaped particles self-assembled into highly porous morphologies. The self-assembly of particles was scrutinized at different reduced temperatures (T*= $k_{\rm B}T/\epsilon_{\rm SS}$, where $k_{\rm B}$ is the Boltzmann constant and $\epsilon_{\rm SS}$ is the depth of the potential well for a pair of central seeds in lobed particles). All lobed particles (except the dumbbell shaped particles) exhibited selfassembly at the lowest T^* (0.4); however, none of them self-assemble at the highest T* (1.0). In another work, 49 we also studied the influence of the lobe size and temperature on the porosity and morphology of the self-assembled superstructures formed by five different types of lobed particles of different shapes (snowman, dumbbell, trigonal planar, square planar, and tetrahedral). These particles self-assembled into crystalline structures, liquid droplets, micelles, random aggregates, spherical aggregates, and two-dimensional sheets, based on the size and temperature. We also showed that the porosity of the self-assembled morphologies, which is a desired characteristic in hydrogel-like with materials, improved an increase temperature.

Given the design of our previously proposed lobed particles, we hypothesized that incorporating a functional group on each lobe will likely create an additional excluded volume around the non-spherical particles that may enhance the porosity in a given self-assembled structure. We tested this hypothesis in this work by conducting coarsegrained Langevin dynamics simulations to elucidate the significance of functionalized lobed particles during self-assembly. We have incorporated functional groups into lobed particles with different shapes reported in our previous work: **48* snowman $(S_1^{\rm SM})$, dumbbell $(S_2^{\rm DB})$, trigonal planar $(S_3^{\rm TP})$, square

planar (S_4^{SP}) , tetrahedral (S_4^{TH}) , trigonal bipyramidal (S_5^{TB}) , and octahedral (S_6^{OC}) , where the values in the superscript and subscript correspond to the shape of the particle and the number of functional groups attached to the lobes in each type of particle, respectively (Fig. 1). We systematically studied the effect of adding functional groups by tuning the interactions between them and the influence of temperature on the porosities of the self-assembled morphologies. The theoretical approach outlined in our work to understand the aggregation propensity of the lobed particles decorated with functional groups is potentially useful in creating porous self-assembled morphologies relevant to hydrogel-like materials.

MODELS AND METHODS

Simulation Setup

We have performed coarse-grained Langevin dynamics simulations in reduced units using the HOOMD-blue open-source particle simulation toolkit. The diameters of the seed $(\sigma_{\rm S})$, lobe $(\sigma_{\rm L})$, and functional group $(\sigma_{\rm F})$ in each particle were set to 2.0, 1.0, and 0.5 in reduced units, respectively. The mass of each seed $(m_{\rm S})$, lobe $(m_{\rm L})$, and functional group $(m_{\rm F})$ was set to 1.0. The harmonic potentials were used to model all bonds and angles in the lobed particles with the force constants $(k_{\rm bond} = k_{\rm angle} = 1000$, in reduced units) aimed to preserve the shapes of lobed particles during simulations. The non-bonded interactions between the seed–seed

(S–S), lobe-lobe (L–L), seed-lobe (S–L), functional group-functional group (F–F), seed-functional group (S–F), and lobe-functional group (L–F) were implemented using the surface shifted Lennard-Jones (SSLJ) potential, given by Eq. 1.

$$V_{SSLJ}(r_{ij}) = \left\{egin{array}{ll} 4\epsilon_{ij}igg[\Big(rac{\sigma}{r_{ij}-\Delta}\Big)^{12} - \Big(rac{\sigma}{r_{ij}-\Delta}\Big)^{6}igg], & ext{when } ext{r}_{ij} < ext{r}_{ ext{cut}} + \Delta \ 0, & ext{when } ext{r}_{ij} \geq ext{r}_{ ext{cut}} + \Delta \ \end{array}
ight.$$

where r_{ij} is the distance between a pair of particles iand j, ϵ_{ij} is the depth of the potential energy well for the *i*–*j* pair, $\Delta = (\sigma_i + \sigma_j)/2 - 1$, where σ_i and σ_j are the diameters of the particles i and j, respectively. The cut-off distance (r_{cut}) between the i-j pairs was set to $2^{1/6}\sigma$ for repulsive S–S, S–L, and S–F pairs. The ϵ_{ij} for the L–L and L–F pairs was set to 3.0 and 4.0 in reduced units, respectively. The attractive interactions between the functional groups on lobes were investigated by evaluating three values for the parameter ϵ_{FF} = 5.0, 6.0, and 7.5. All simulations were performed at five different temperature values $(k_{\rm B}T=0.8,\,0.9,\,1.0,\,1.1,\,{\rm and}\,\,1.2).$ Thus, each of the seven types of lobed particles was simulated at five different temperatures and three ϵ_{FF} values resulting in a total of 105 simulations. We carried out all simulations in cubical simulation domains (200 σ_L × $200\sigma_L \times 200\sigma_L$) with the periodic boundary conditions, where each system was comprised of 15,625 particles. Each system was simulated for 10⁸ steps with a time step of 0.005.

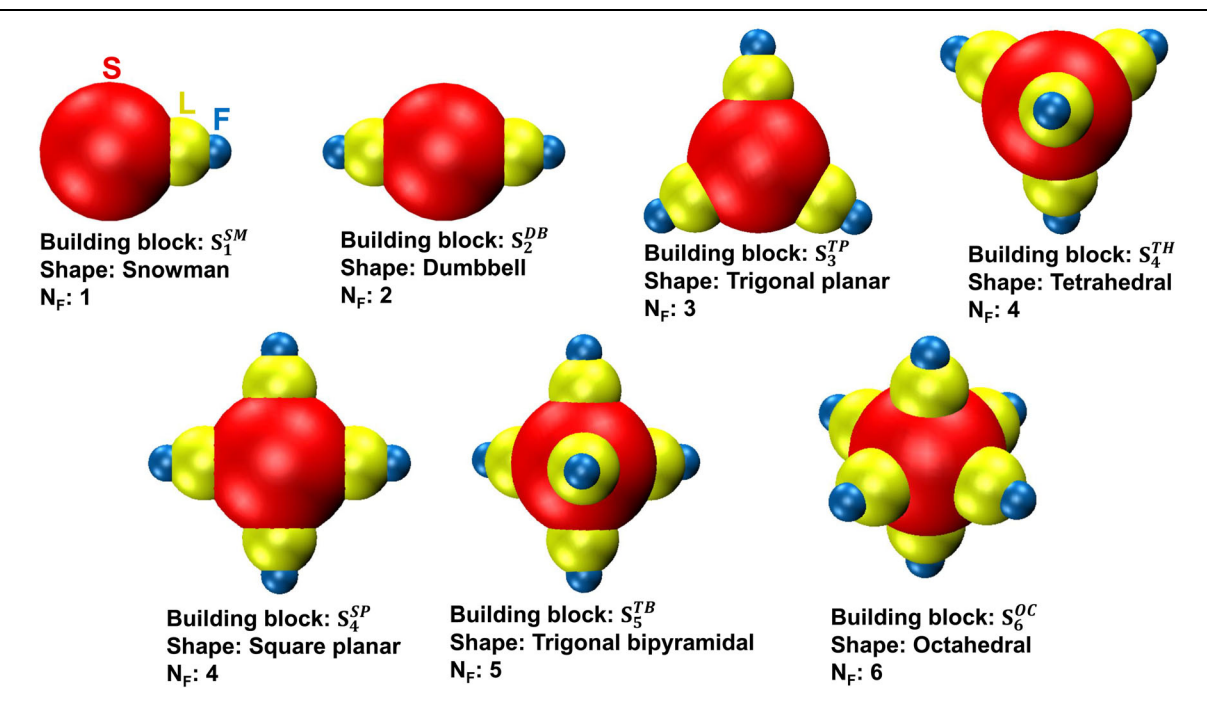


Fig. 1. Seven types of functionalized lobed particles studied in this work are shown. The central seed (S), the lobe (L), and the functional group (F) in each particle are represented by red, yellow, and blue spheres, respectively. The diameters of 'S,' 'L,' and 'F' are 2, 1, and 0.5 in reduced units, respectively. The number of functional groups are denoted by N_F (Color figure online).

Morphology Analysis

The analyses of the radial distribution function (RDF) for the seed–seed pair and qualitative visual inspections using the VMD software were employed to characterize morphologies of the self-assembled structures. Specifically, the structures were classified into seven different categories, listed here alphabetically: cylindrical aggregates, dissociated states, elongated chains, honeycomb aggregates, honeycomb sheets, random aggregates, and square sheets. The structures with the dissociated states are those where self-assembly is not observed. Similar to our previous work, and the RDF is calculated using Eq. 2, where $\rho(r)$ is the density of particles at a distance r from the reference particle and ρ_0 is the bulk density.

$$g(r) = \frac{\rho(r)}{\rho_0} \tag{2}$$

Porosity Analysis

After extracting the largest possible cuboids from the three-dimensional self-assembled structures, the Zeo++ software $^{52-54}$ was used to compute the pore size distributions (PSD) and to estimate the diameter of the largest free sphere (D_{LFS}) that can diffuse through the porous structure. A probe with the radius equivalent to $\frac{1}{2}\sigma_L$ was used for the PSD calculations. This value is consistent with our previous work. 48,49

RESULTS

Self-Assembled Morphologies

An understanding of the morphologies of self-assembled structures at different temperatures and interaction parameters is needed to design lobed particles with desired characteristics. In Fig. 2, we show the phase behavior for seven types of

functionalized lobed particles at various temperatures and varied interaction strengths between the functional groups (ϵ_{FF}) . We observed that the functionalized lobed particles self-assembled into distinct morphologies including cylindrical aggregates, elongated chains, honeycomb aggregates, honeycomb sheets, random aggregates, and square sheets, except the $S_1^{\rm SM}$ particles that exist in a dissociated state at all simulation conditions.

We observed that the particle shapes with a higher number of functional lobes form self-assembled aggregates at higher temperatures. The S_5^{TB} and S_6^{OC} particles self-assembled into a random aggregate morphology but the S_4^{SP} particles formed square sheets at all simulation conditions. The transformation from cylindrical aggregates to random aggregates for the S_4^{TH} ($k_{\rm B}T$ = 1.1 and 1.2 at ϵ_{FF} = 6) particles was observed at a higher temperature for higher ϵ_{FF} values ($k_{\rm B}T$ = 1.1 and 1.2 at ϵ_{FF} = 7.5). The S_4^{TH} particles exhibited a dissociated state only at $k_{\rm B}T$ = 1.2 with ϵ_{FF} = 5. For S_3^{TP} particles, we observed a transition in the morphology from honeycomb sheets to honeycomb aggregates and to a dissociated state with an increase in temperature for each ϵ_{FF} . We also observed a transition for S_2^{DB} particles from the elongated chain-like structures to a dissociated state with an increase in temperature. Thus, the functionalized lobed particles self-assembled into distinct morphologies with an increase in the number of functional lobes, and the rate of selfassembly is proportional to interactions between the functional groups: 66%, 71%, and 77% of selfassembled structures are observed at the ϵ_{FF} values of 5 (Fig. 2a), 6 (Fig. 2b), and 7.5 (Fig. 2c), respectively.

Average Potential Energy

The average potential energy per particle $(\langle E_p \rangle)$ at different simulation temperatures $(k_{\rm B} {\rm T})$ and varied interactions between the functional lobes (ϵ_{FF}) were examined to probe the stability of the self-assembled morphologies (Fig. 3). We noticed that $\langle E_p \rangle$

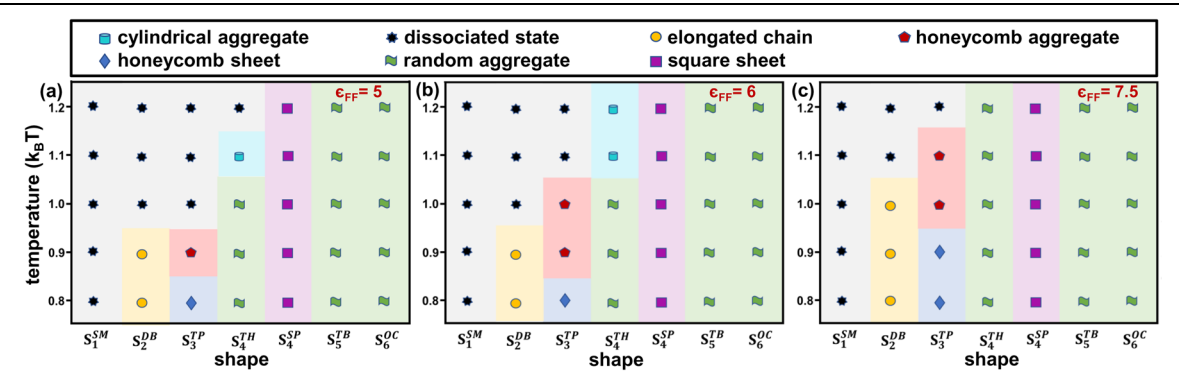


Fig. 2. Phase behavior of functionalized lobed particles at different temperatures is shown for (a) $\epsilon_{FF} = 5$, (b) $\epsilon_{FF} = 6$, and (c) $\epsilon_{FF} = 7.5$, where ϵ_{FF} signifies the attractive interactions between the functional groups on lobes. The morphologies shown are cylindrical aggregates (cyan cylinders), dissociated states (black stars), elongated chains (orange circles), honeycomb aggregates (red pentagons), honeycomb sheets (blue diamonds), random aggregates (green waves), and square sheets (purple squares) (Color figure online).

decreases with an increase in the number of functional groups leading to energetically-driven selfassembled superstructures. The dumbbell shaped particles (with one functional group) and octahedral particles (with six functional groups) have the highest and the lowest values of $\langle E_p \rangle$, respectively. Specifically, the snowman and dumbbell shaped particles with a lower number of functional groups (< 3) have higher mean potential energy. At the highest $k_{\rm B}{\rm T}$ (= 1.2), they possess positive $\langle E_p\rangle$ implying an unstable system due to enhanced diffusion of particles in the simulation domain. At lower $k_{\rm B}{
m T}$ values (< 1.0), the $\langle E_p
angle$ values calculated for the dumbbell shaped particles are lower (< -5 units), which indicates a stable self-assembled system. We noted earlier that the dumbbell shaped particles attain stable self-assemblies with an elongated chain morphology at lower $k_{\rm B}T$. Interestingly, in most of the cases the particles with three or more functional groups exhibited distinct self-assembled morphologies when $\langle E_p \rangle < -10.5$ units although these particles fail to self-assemble when $\langle E_p \rangle > -$ 10.5 units. Thus, we found that $\langle E_p \rangle$ at a value of 10.5 units is a decisive parameter for the morphological transitions from disordered states to selfassembled structures for the particles with three or more functional groups. The $\langle E_p \rangle$ values also reduce with an increase in the interaction strength between the functional groups, which suggests stable self-assembled structures.

Structural Motifs in Self-Assembled Structures

We further characterized self-assembled morphologies by inspecting their key structural motifs. We observed that S_2^{DB} particles self-assemble into one-dimensional morphologies, while S_3^{TP} and S_4^{SP} particles form two-dimensional structures (Fig. 4). The S_2^{DB} particles acquire dissociated states at $k_{
m B}{
m T}$ > 0.9 at the ϵ_{FF} values of 5 and 6. However, with a higher ϵ_{FF} value of 7.5 their self-assembly is observed at $k_BT = 1.0$, but a dissociated state is seen on further increasing the temperature ($k_{\rm B}T$ > 1.0). The functional groups on the S_2^{DB} particles rearrange themselves to exhibit elongated chainlike structures (Fig. 4a). For the same ϵ_{FF} value, the peak height observed in the RDF between the seed particles, $g_{SS}(r)$, gradually decreases with an increase in temperature which implies that the probability of finding another seed in the immediate vicinity of the central seed is reducing with the temperature. This observation further reveals that the length of the elongated chains may gradually shorten with an increase in temperature. Moreover, the $g_{SS}(r)$ peaks, at the same k_BT value, marginally increase with an increase in the ϵ_{FF} value indicating that the number density of availability of other seeds around the central seed is proportional to the

 ϵ_{FF} value.

The S_3^{TP} particles self-assemble to form superstructures composed of honeycomb units (Fig. 4b). At the lowest $k_B T$ value, S_3^{TP} particles exhibit a honeycomb sheet morphology, where the central

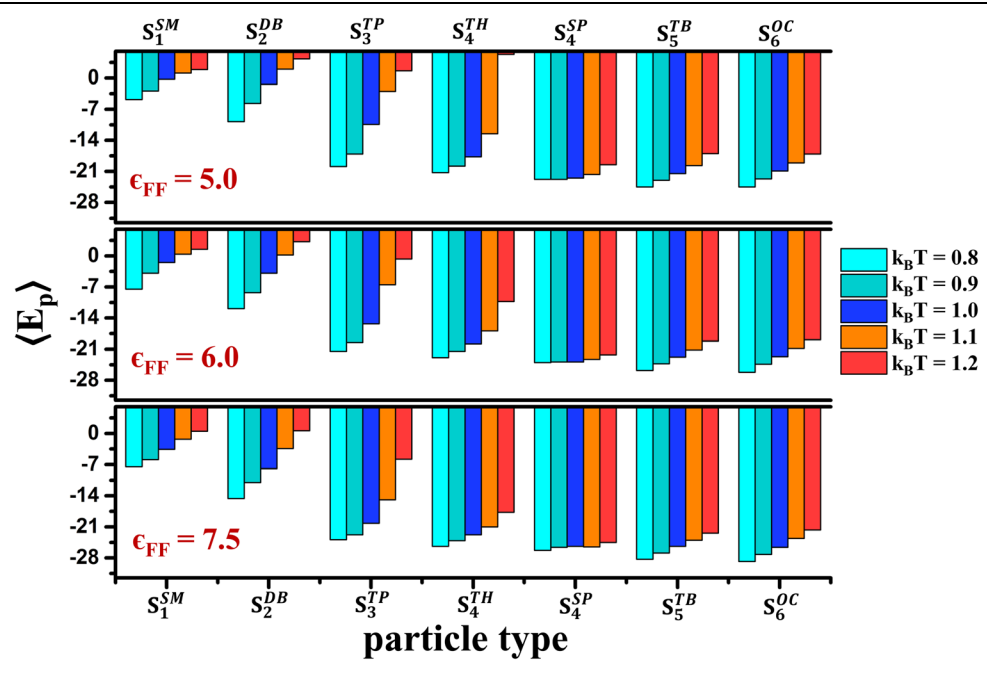


Fig. 3. Average potential energy per particle $(\langle E_p \rangle)$. The per residue potential energy of each system averaged over the simulation time for all particles at different temperatures and ϵ_{FF} values are represented by stacked bar plots. The potential energies in all systems were calculated at $k_{\rm B}$ T of 0.8 (cyan), 0.9 (dark cyan), 1.0 (blue), 1.1 (orange), and 1.2 (red) values. The potential energy of each system at the ϵ_{FF} values of 5.0, 6.0, and 7.5 is shown in the top, middle, and bottom panels, respectively (Color figure online).

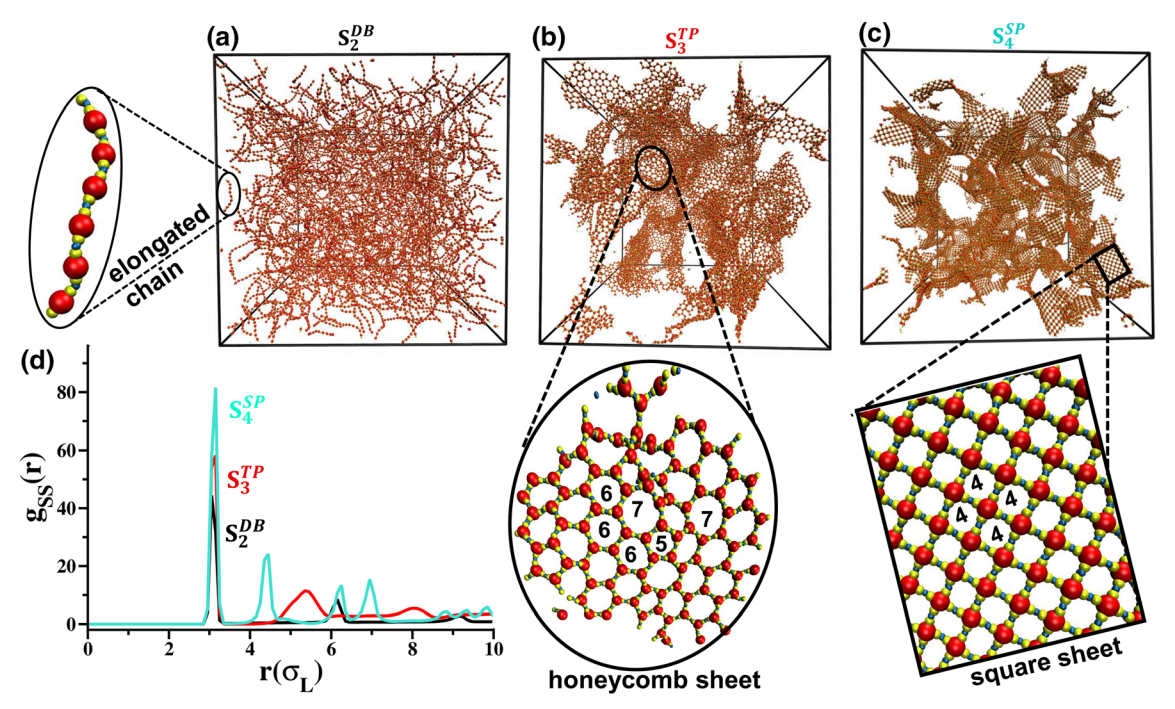


Fig. 4. One- and two-dimensional self-assembled morphologies at different conditions. (a) Elongated chain, (b) honeycomb sheet, and (c) square sheet morphologies are obtained for the dumbbell (S_2^{DB}), trigonal planar (S_3^{TP}) and square planar (S_3^{SP}) particles, respectively. The zoomed views of structural motifs of the self-assembled morphologies are shown. The structural motif in the honeycomb sheets is constituted by a 5-, 6-, and 7-membered ring arrangement of S_4^{TP} particles. The structural motif in the square sheets is constituted by a square-like arrangement of S_4^{SP} particles. (d) The RDF curves for S_2^{DB} , S_3^{TP} , and S_4^{SP} shaped particles are shown in black, red, and cyan lines, respectively (Color figure online).

seeds resemble the vertices of a hexagonal ring unit. The peaks of the $g_{\rm SS}({\bf r})$ obtained for the S_3^{TP} particles show trends similar to the $g_{\rm SS}({\bf r})$ of S_2^{DB} , as the peak height reduces with an increase in temperature and results in structural transitioning. For example, S_3^{TP} (with ϵ_{FF} = 5) particles exhibited a honeycomb sheet morphology at $k_BT = 0.8$, honeycomb aggregate morphology at $k_BT = 0.9$, and a dissociated state at $k_B T \geq 1.0$. However, the peaks in the $g_{SS}(r)$ for S_4^{SP} particles show a reverse trend in comparison to particles show a reverse tient in comparison $g_{\rm SS}({\bf r})$ of S_2^{DB} and S_3^{TP} particles (Fig. S1). The heights of the peaks reduce with an increase in temperature for the S_2^{DB} and S_3^{TP} particles, but in contrast the $g_{\rm SS}({\bf r})$ peak heights for S_4^{SP} particles increase with an increase of temperature (Fig. S1c). Thus, the S_4^{SP} particles maintain a square sheet morphology at all $k_B T$ and ϵ_{FF} values (Fig. 4c). Moreover, the size of square sheets formed by the S_4^{SP} particles at a higher temperature ($k_B T = 1.2$) are larger in comparison to the size of self-assembled square sheets formed at a lower temperature ($k_BT=0.8$) (Fig. S2). This observation is due to the higher density of lobed particles in each coordination shell at higher temperature, as noticed from the $g_{SS}(r)$ plot (Fig. S2c).

We further analyzed the pattern of two-dimensional sheets formed by S_3^{TP} and S_4^{SP} particles. Interestingly, the structural motif of the honeycomb sheet-like structure formed by the S_3^{TP} particles is

mainly constituted by six-membered rings and partly by five- and seven-membered rings (zoomed view in Fig. 4b). However, a four-membered square ring formed by the four units of the S_4^{SP} particles (zoomed view in Fig. 4c) is the sole structural motif of the square planar sheets. We suggest that the variability in the structural motif allows a higher conformational degree of freedom, thereby affording a relatively higher curvature for the sheets formed by the S_3^{TP} particles compared to the self-assembled sheets formed by the S_4^{SP} particles.

Three-Dimensional Self-Assemblies

We now describe the details of the self-assembled morphologies formed by the non-planar particles, i.e., S_4^{TH} , S_5^{TB} , and S_6^{OC} shaped particles. The S_4^{TH} particles self-assembled into random aggregates, a concoction of varied types of morphologies, at the ϵ_{FF} value of 7.5. At a lower ϵ_{FF} value of 5, the random aggregates (for $k_B T = 0.8$ –1.0) undergo a transition to cylindrical aggregates (at $k_B T = 1.1$) and then to a disordered state ($k_B T = 1.2$). At an intermediate ϵ_{FF} value of 6, we observed distinct structural transitions for the S_4^{TH} particles (Fig. 5). The random aggregates with branched morphologies are observed at a lower range of $k_B T = 0.8$ –1.0 (Fig. 5a). However, the random aggregates partially segregated into cylindrical aggregates at $k_B T = 1.1$ (Fig. 5b) at the ϵ_{FF} value of 6. We observed that the

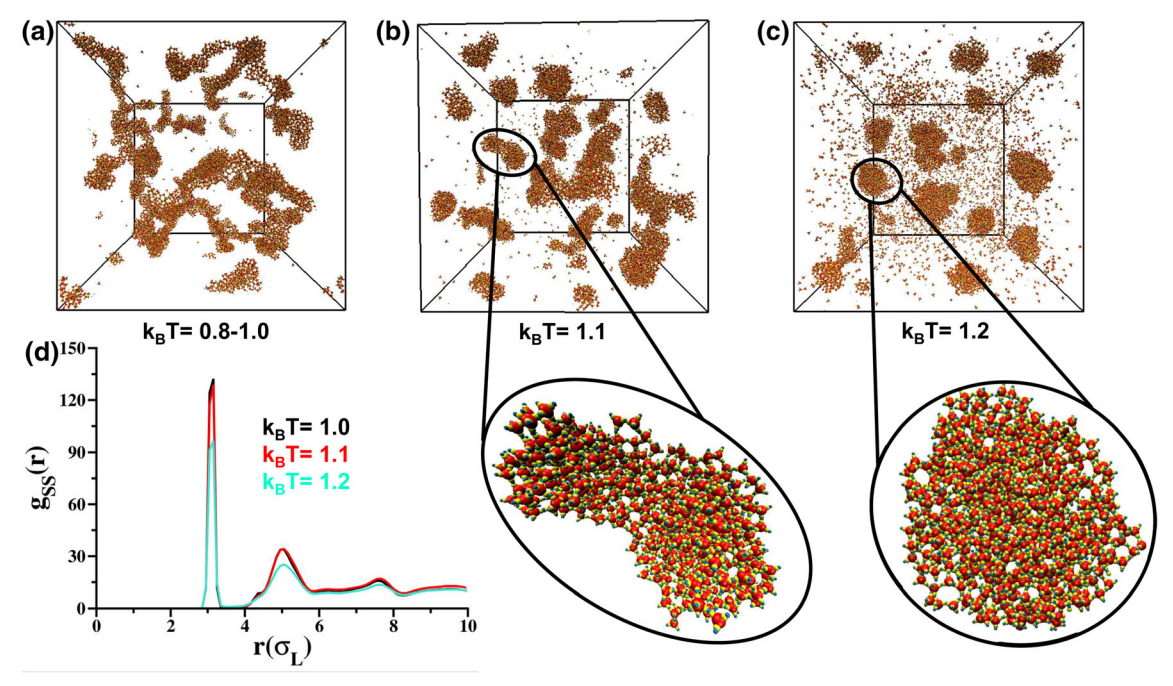


Fig. 5. Self-assembly of tetrahedral shaped lobed particles at $\epsilon_{FF} = 6$. The assembled morphologies of tetrahedral shaped lobed particles into (a) random aggregates, (b) cylindrical aggregates, and (c) a blend of cylindrical and spherical aggregates at $k_BT \le 1.0$, $k_BT = 1.1$ and $k_BT = 1.2$, respectively, is depicted. The zoomed views of the cylindrical and spherical aggregates are shown. (d) The RDF curves at k_BT values of 1.0, 1.1 and 1.2 are shown in black, red, and cyan lines, respectively (Color figure online).

second and third peaks of the $g_{\rm SS}({\bf r})$ curves at $k_B{\rm T}$ of 1.0 and 1.1 are nearly identical and the first intense peak at $k_B{\rm T}=1.0$ is marginally lower than that of the first intense peak at $k_B{\rm T}=1.1$ (Fig. 5d), which is plausible for the structural transitioning from random aggregates to cylindrical aggregates. At the highest temperature ($k_B{\rm T}=1.2$), we observed distinct cylindrical as well as spherical aggregates (Fig. 5c) at the ϵ_{FF} value of 6. The first and the second peaks in the $g_{\rm SS}({\bf r})$ curve are significantly lower at $k_B{\rm T}=1.2$, likely due to the increased diffusion of particles at higher temperatures.

diffusion of particles at higher temperatures. The S_5^{TB} and S_6^{OC} shaped lobed particles self-assemble into similar random aggregate morphologies. We did not observe any significant morphological phase transitions in these particles as they selfassemble under all simulation conditions. The peaks obtained from the $g_{SS}(\mathbf{r})$ calculation for both types of particles are similar, although the S_6^{OC} particles which have more functional groups exhibited a higher density of lobed particles in their three coordination shells compared to the S_5^{TB} particles. At lower temperatures, the random aggregates formed by both types of particles are similar in size and gradually inflate with an increase in temperature (Figs. S3 and S4). The height of the first $g_{SS}(r)$ peak for S_5^{TB} and S_6^{OC} particles sequentially decreases with an increase in temperature, but the second and third peaks marginally increase with an increase in temperature (Figs. S3f and S4f), thereby indicating the formation of an inflated self-assembled structure at higher temperatures.

Porosity Analysis

The self-assembled structures were further characterized for their porosities after extracting the largest possible cuboids from the three-dimensional structures formed at the three ϵ_{FF} values evaluated in this study. It is worth noting that these cuboids can only be extracted for the structures formed by the self-assembly of S_3^{TP} , S_4^{TH} , S_5^{TB} , and S_6^{OC} particles, since these were the only particles that formed three-dimensional aggregates.

The pore size distribution (PSD) plots (Fig. S5) indicate that the structures formed by the S_5^{TB} and S_6^{OC} particles have pores that are smaller and more homogeneous in pore diameters $(2.0\sigma_L-4.7\sigma_L)$, and $1.7\sigma_L-3.8\sigma_L$, respectively) when compared to the structures formed by S_3^{TP} and S_4^{TH} particles $(4.0\sigma_L-10.5\sigma_L)$, and $3.0\sigma_L-6.2\sigma_L$, respectively) at $\epsilon_{FF}=5.0$ (Fig. S5a). We also observed that an increase in ϵ_{FF} leads to broader pore size distributions for the S_5^{TB} and S_6^{OC} particles, indicating that their self-assembled structures have pores that are larger in size and more heterogeneous at those conditions (Fig. S5). For instance, at $\epsilon_{FF}=7.5$ (Fig. S5c), the PSD ranges for the S_5^{TB} and S_6^{OC} particles widen to $2.0\sigma_L-5.3\sigma_L$, and $1.8\sigma_L-4.5\sigma_L$, respectively.

The porosity of each self-assembled structure was also compared using the diameter of the largest free sphere (D_{LFS}) as a metric (Fig. 6). We observed that the addition of functional groups to the lobes resulted in a significant increase in the porosities

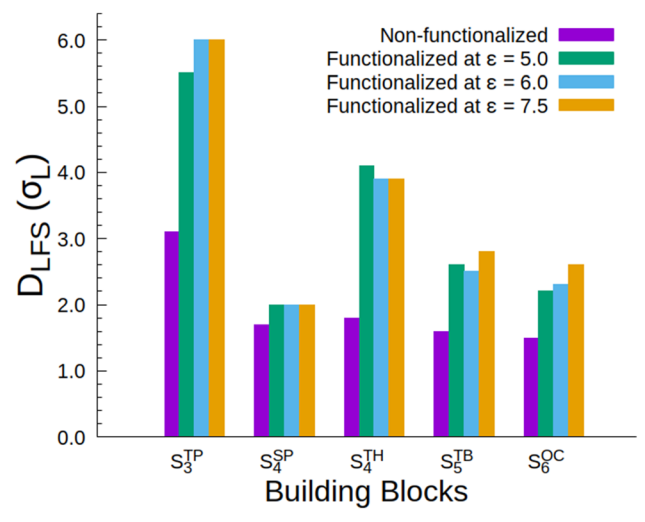


Fig. 6. Porosity of self-assembled structures as characterized via the diameter of the largest free sphere (D_{LFS}). A comparison of the porosities of self-assembled structures, as measured by D_{LFS} , is shown for particles with functionalized lobes and non-functionalized lobes. The data for non-functionalized particles are based on our previous work.⁴⁸

of the self-assembled structures compared to the structures formed in our previous work, where the lobes were not functionalized. The highest porosity in this study was observed for the aggregates formed by the S_3^{TP} particles $(D_{LFS}=6.0\sigma_L)$, followed by the S_4^{TH} particles $(D_{LFS}=4.0\sigma_L)$, the S_5^{TB} particles $(D_{LFS}=2.8\sigma_L)$, the S_4^{OC} particles $(D_{LFS}=2.6\sigma_L)$, and the S_4^{SP} particles $(D_{LFS}=2.0\sigma_L)$. We conclude that the porosities in the three-dimensional structures formed by the self-assembly of these particles are inversely proportional to the number of lobes in the particle, except for the S_4^{SP} particles which form the least porous structures due to a tighter packing in the square sheet morphology.

DISCUSSION

The fabrication of patchy particles with diverse anisotropic functional motifs has utility in forming three-dimensional scaffolds for various applications.^{5,6,8,55} In the current study, we have elucidated the ability of seven different types of functionalized lobed particles to self-assemble into superstructures with distinct morphologies. The magnitude of attractive interactions between the functional groups incorporated in the lobes and the temperature are chief attributes that regulate the size, morphology, porosity, and phase behavior of self-assembled structures. The selection of the r_{cut} value in MD simulation is also an indispensable parameter that governs the morphology and porosity of the self-assembled structures. The value of r_{cut} can be adjusted to tune the excluded volume interactions between the colloidal particles. In our

study, the L-L, F-L, and F-F pairs were made attractive, whereas the interactions among S-S, S-L, and S-F pairs were made purely repulsive after setting r_{cut} to the $2^{1/6}\sigma$ value. The purely repulsive potential minimizes the interaction radius, eventually reducing the interacting pairs to 5–6. To model both repulsive and attractive interactions or shortrange attractive hydrophobic interactions, one may set the r_{cut} to 2.5σ value. The repulsive r_{cut} value may generate larger morphologies with higher porosity and one may observe compact self-assembled structures at higher r_{cut} value of 2.5σ . The propensity of lobed particles to self-assemble enhances by increasing the number of functional lobes as well as by tuning the attractive interactions between them. The interactions between the functional groups may be tuned to explore the effect of a wide range of weak (e.g., hydrogen bonding, dipoledipole interactions, dispersion forces, p-stacking, metallophilic, or hydrophobic/hydrophilic interactions) to strong (e.g., ionic bonds or covalent bonds driven by photoresponsive motifs and electromagnetic excitations 57,58) intermolecular interactions on the physicochemical properties of the self-assembled structure. The dumbbell and trigonal planar particles with two and three functional groups, respectively, are unable to assemble at higher temperatures, rather particles with more functional groups (≥ 4) exhibited self-assembly at a wider temperature range.

We also tallied our results with our earlier simulation study performed on lobed particles with similar shapes but without the functional groups on lobes. 48 In the previous study, we observed that the self-assembly of the non-functionalized lobed particles were obtained mostly at lower temperatures $(k_{\rm B}T<0.7)$ compared to the functionalized lobed particles where we observed that the particles selfassemble over a wider range of temperatures (0.8) $\leq k_{\rm B} {
m T} \leq 1.2$). The lobed particles without functional groups self-assemble into porous and crystalline structures. However, we observed highly non-crystalline porous self-assembled structures for lobed particles with the functional groups. Notably, the porosity analysis reveals the diameter of the largest free sphere (D_{LFS}) for each self-assembled structure. The D_{LFS} values for the functionalized lobed particles are significantly higher than those for nonfunctionalized particles reported in our previous work.⁴⁹ As an example, the D_{LFS} values calculated for the functionalized S_3^{TP} and S_4^{TH} self-assembled structures are doubled compared to the non-functionalized self-assembled structures (Fig. 6).

Based on our results, we propose that the functionalized S_3^{TP} and S_4^{TH} lobed particles are the most suitable candidates for designing porous, biodegradable, and biocompatible self-assembled morphologies for applications in tissue engineering. The hydrogels formed by the functional lobed particles

may be tailored to meet specific requirements in biomedical engineering. Specifically, the functional lobes with higher interaction strengths may generate highly porous and mechanically stable matrices appropriate for cell growth and migration. ^{31,32} The surface area of the functionalized hydrogels could be tuned to stimulate drugs and biomolecules adsorption for targeted drug and gene delivery, respectively. We conclude that the lobed particles with the functional groups substantially enhanced the porosities of the assembled superstructures compared to the non-functionalized self-assembled structures. Importantly, the self-assemblies of the functionalized S_3^{TP} particles are highly porous and interconnected with enhanced mechanical stability, which makes such assemblies a compatible microenvironment for optimal cell growth and function.

ACKNOWLEDGEMENTS

The financial support provided by the National Science Foundation (NSF) EPSCoR award (OIA-1757371; H.V.) is gratefully acknowledged. We also acknowledge computational support through the BioMade supercomputer, a heterogeneous CPU/GPU cluster at the University of New Hampshire provided by the NSF EPSCoR award (OIA-1757371; H.V.).

CONFLICT OF INTEREST

The authors declare that they have no conflict of interest.

OPEN ACCESS

This article is licensed under a Creative Commons Attribution 4.0 International License, which permits use, sharing, adaptation, distribution and reproduction in any medium or format, as long as you give appropriate credit to the original author(s) and the source, provide a link to the Creative Commons licence, and indicate if changes were made. The images or other third party material in this article are included in the article's Creative Commons licence, unless indicated otherwise in a credit line to the material. If material is not included in the article's Creative Commons licence and your intended use is not permitted by statutory regulation or exceeds the permitted use, you will need to obtain permission directly from the copyright holder. To view a copy of this licence, visit h ttp://creativecommons.org/licenses/by/4.0/.

SUPPLEMENTARY INFORMATION

The online version contains supplementary material available at https://doi.org/10.1007/s11837-021-04715-w.

REFERENCES

- Z. Zhang, S.C. Glotzer, Self-assembly of patchy particles. Nano Lett. 4(8), 1407–1413 (2004).
- F. Li, D.P. Josephson, A. Stein, Colloidal assembly: the road from particles to colloidal molecules and crystals. Angew. Chem. Int. Ed. 50(2), 360–388 (2011).
- 3. S.C. Glotzer, M.J. Solomon, Anisotropy of building blocks and their assembly into complex structures. Nat. Mater. **6**(8), 557–562 (2007).
- D. Morphew, J. Shaw, C. Avins, D. Chakrabarti, Programming hierarchical self-assembly of patchy particles into colloidal crystals via colloidal molecules. ACS Nano 12(3), 2355–2364 (2018).
- W. Li, H. Palis, R. Mérindol, J. Majimel, S. Ravaine, E. Duguet, Colloidal molecules and patchy particles: complementary concepts, synthesis and self-assembly. Chem. Soc. Rev. 49(6), 1955–1976 (2020).
- A. Kim, L. Yao, F. Kalutantirige, S. Zhou, Q. Chen, Patchy Nanoparticle Synthesis and Self-Assembly (In Self-Assembly of Nanostructures, IntechOpen, 2020).
- Z. Gong, T. Hueckel, G.-R. Yi, S. Sacanna, Patchy particles made by colloidal fusion. Nature 550(7675), 234–238 (2017).
- 8. E. Elacqua, X. Zheng, C. Shillingford, M. Liu, M. Weck, Molecular recognition in the colloidal world. Acc. Chem. Res. **50**(11), 2756–2766 (2017).
- S. Wintzheimer, T. Granath, M. Oppmann, T. Kister, T. Thai, T. Kraus, N. Vogel, K. Mandel, Supraparticles: functionality from uniform structural motifs. ACS Nano 12(6), 5093-5120 (2018).
- A. Walther, A.H.E. Muller, Janus particles: synthesis, self-assembly, physical properties, and applications. Chem. Rev. 113(7), 5194–5261 (2013).
- T. Hueckel, G.M. Hocky, J. Palacci, S. Sacanna, Ionic solids from common colloids. Nature 580(7804), 487–490 (2020).
- S. Ravaine, E. Duguet, Synthesis and assembly of patchy particles: recent progress and future prospects. Curr. Opin. Colloid Interface Sci. 30, 45–53 (2017).
- R. Mérindol, E. Duguet, S. Ravaine, Synthesis of colloidal molecules: recent advances and perspectives. Chem. Asian J. 14(19), 3232–3239 (2019).
- D. Morphew, D. Chakrabarti, Clusters of anisotropic colloidal particles: from colloidal molecules to supracolloidal structures. Curr. Opin. Colloid Interface Sci. 30, 70–80 (2017).
- K.H. Ku, J.M. Shin, H. Yun, G.-R. Yi, S.G. Jang, B.J. Kim, Multidimensional design of anisotropic polymer particles from solvent-evaporative emulsion. Adv. Funct. Mater. 28(42), 1802961 (2018).
- A.B. Pawar, I. Kretzschmar, Fabrication, assembly, and application of patchy particles. Macromol. Rapid Commun. 31(2), 150–168 (2010).
- Q. Chen, J. Yan, J. Zhang, S.C. Bae, S. Granick, Janus and multiblock colloidal particles. Langmuir 28(38), 13555– 13561 (2012).
- S. Sacanna, M. Korpics, K. Rodriguez, L. Colón-Meléndez, S.-H. Kim, D.J. Pine, G.-R. Yi, Nat. Commun. Shaping colloids for self-assembly 4(1), 1–6 (2013).
- B. Peng, H.R. Vutukuri, A. van Blaaderen, A. Imhof, Synthesis of fluorescent monodisperse non-spherical Dumbbell-like model colloids. J. Mater. Chem. 22(41), 21893–21900 (2012).
- D.J. Kraft, W.S. Vlug, C.M. van Kats, A. van Blaaderen, A. Imhof, W.K. Kegel, Self-assembly of colloids with liquid protrusions. J. Am. Chem. Soc. 131(3), 1182–1186 (2009).
- C.I. Zoldesi, C.A. van Walree, A. Imhof, Deformable hollow hybrid silica/siloxane colloids by emulsion templating. Langmuir 22(9), 4343–4352 (2006).
- E. Chiellini, A. Corti, S. D'Antone, R. Solaro, Biodegradation of poly (vinyl alcohol) based materials. Prog. Polym. Sci. 28(6), 963-1014 (2003).
- C.C. DeMerlis, D.R. Schoneker, Review of the oral toxicity of polyvinyl alcohol (pva). Food Chem. Toxicol. 41(3), 319–326 (2003).

- S.-F. Chong, A.A.A. Smith, A.N. Zelikin, Microstructured, functional pva hydrogels through bioconjugation with oligopeptides under physiological conditions. Small 9(6), 942–950 (2013).
- J.D. Weaver, D.N. Ku, Mechanical evaluation of polyvinyl alcohol cryogels for covered stents. J. Med. Devices 4(3), 1 (2010).
- F. Rossi, R. Ferrari, F. Castiglione, A. Mele, G. Perale, D. Moscatelli, Polymer hydrogel functionalized with biodegradable nanoparticles as composite system for controlled drug delivery. Nanotechnology 26(1), 015602 (2014).
- S. Motamed, M.P. Del Borgo, K. Kulkarni, N. Habila, K. Zhou, P. Perlmutter, J.S. Forsythe, M.I. Aguilar, A self-assembling β-peptide hydrogel for neural tissue engineering. Soft Matter 12(8), 2243–2246 (2016).
- S.C. Neves, R.F. Pereira, M. Araújo, C.C. Barrias, Bioengineered peptide-functionalized hydrogels for tissue regeneration and repair, in *Peptides and proteins as biomaterials for tissue regeneration and repair*, pp. 101–125 (Elsevier, 2018).
- S. Yigit, R. Sanyal, A. Sanyal, Fabrication and functionalization of hydrogels through "click" chemistry. Chem. Asian J. 6(10), 2648–2659 (2011).
- J.M. Ino, P. Chevallier, D. Letourneur, D. Mantovani, C.L. Visage, Plasma functionalization of poly (vinyl alcohol) hydrogel for cell adhesion enhancement. Biomatter 3(4), e25414 (2013).
- Y. Wang, W. Zhang, C. Gong, B. Liu, Y. Li, L. Wang, S. Zhiqiang, G. Wei, Recent advances in the fabrication, functionalization, and bioapplications of peptide hydrogels. Soft Matter 16(44), 10029–10045 (2020).
- K. Elkhoury, C.S. Russell, L. Sanchez-Gonzalez, A. Mostafavi, T.J. Williams, C. Kahn, N.A. Peppas, E. Arab-Tehrany, A. Tamayol, Soft-nanoparticle functionalization of natural hydrogels for tissue engineering applications. Adv. Healthcare Mater. 8(18), 1900506 (2019).
- P.A. Lovell, F.J. Schork, Fundamentals of emulsion polymerization. Biomacromolecules 21(11), 4396

 –4441 (2020).
- 34. J. Brijitta, P. Schurtenberger, Responsive hydrogel colloids: Structure, interactions, phase behavior, and equilibrium and nonequilibrium transitions of microgel dispersions. Curr. Opin. Colloid Interface Sci. 40, 87–103 (2019).
- Y. Wang, Y. Wang, D.R. Breed, V.N. Manoharan, L. Feng, A.D. Hollingsworth, M. Weck, D.J. Pine, Colloids with valence and specific directional bonding. Nature 491(7422), 51–55 (2012).
- A. Klinkova, H. Thérien-Aubin, R.M. Choueiri, M. Rubinstein, E. Kumacheva, Colloidal analogs of molecular chain stoppers. Proc. Natl. Acad. Sci. USA 110(47), 18775–18779 (2013).
- R. Schreiber, I. Santiago, A. Ardavan, A.J. Turberfield, Ordering gold nanoparticles with dna origami nanoflowers. ACS Nano 10(8), 7303–7306 (2016).
- J. Zidek, A. Milchev, J. Jancar, T.A. Vilgi, Deformation-induced damage and recovery in model hydrogels-a molecular dynamics simulation. J. Mech. Phys. Solids 94, 372–387 (2016).
- E.S. Minina, P.A. Sánchez, C.N. Likos, S.S. Kantorovich, The influence of the magnetic filler concentration on the properties of a microgel particle: zero-field case. J. Magn. Magnet. Mater. 459, 226–230 (2018).
- I. Adroher-Benítez, A. Martín-Molina, S. Ahualli, M. Quesada-Pérez, G. Odriozola, A. Moncho-Jordá, Competition between excluded-volume and electrostatic interactions for

- nanogel swelling: effects of the counterion valence and nanogel charge. Phys. Chem. Chem. Phys. **19**(9), 6838–6848 (2017).
- S.K. Smoukov, S. Gangwal, M. Marquez, O.D. Velev, Reconfigurable responsive structures assembled from magnetic Janus particles. Soft Matter 5(6), 1285–1292 (2009).
- F. Sciortino, A. Giacometti, G. Pastore, Phase diagram of Janus particles. Phys. Rev. Lett. 103(23), 237801 (2009).
- Z.-W. Li, L. Zhong-Yuan, Z.-Y. Sun, L.-J. An, Model, self-assembly structures, and phase diagram of soft Janus particles. Soft Matter 8(25), 6693–6697 (2012).
- H. Jing, S. Zhou, Y. Sun, X. Fang, W. Limin, Fabrication, properties and applications of Janus particles. Chem. Soc. Rev. 41(11), 4356–4378 (2012).
- A.W. Wilber, J.P.K. Doye, A.A. Louis, Self-assembly of monodisperse clusters: Dependence on target geometry. J. Chem. Phys. 131(17), 11B601 (2009).
- C.R. Iacovella, S.C. Glotzer, Complex crystal structures formed by the self-assembly of ditethered nanospheres. Nano Lett. 9(3), 1206–1211 (2009).
- 47. E. Jankowski, S.C. Glotzer, A comparison of new methods for generating energy-minimizing configurations of patchy particles. J. Chem. Phys. **131**(10), 104104 (2009).
- S. Paul, H. Vashisth, Self-assembly of lobed particles into amorphous and crystalline porous structures. Soft Matter 16(5), 1142–1147 (2020).
- S. Paul, H. Vashisth, Self-assembly behavior of experimentally realizable lobed patchy particles. Soft Matter 16(35), 8101–8107 (2020).
- J.A. Anderson, J. Glaser, S.C. Glotzer, Hoomd-blue: A python package for high-performance molecular dynamics and hard particle monte carlo simulations. Comput. Mater. Sci. 173, 109363 (2020).
- W. Humphrey, A. Dalke, K. Schulten, Vmd: visual molecular dynamics. J. Mol. Graphics 14(1), 33–38 (1996).
- T.F. Willems, C.H. Rycroft, M. Kazi, J.C. Meza, M. Haranczyk, Algorithms and tools for high-throughput geometrybased analysis of crystalline porous materials. Microp. Mesop. Mater. 149(1), 134–141 (2012).
- M. Pinheiro, R.L. Martin, C.H. Rycroft, A. Jones, E. Iglesia, M. Haranczyk, Characterization and comparison of pore landscapes in crystalline porous materials. J. Mol. Gr. Modell. 44, 208–219 (2013).
- M. Pinheiro, R.L. Martin, C.H. Rycroft, M. Haranczyk, High accuracy geometric analysis of crystalline porous materials. CrystEngComm 15(37), 7531–7538 (2013).
- Q.L. Loh, C. Choong, Three-dimensional scaffolds for tissue engineering applications: role of porosity and pore size. Tissue Eng. Part B: Rev. 19(6), 485–502 (2013).
- A.E. Likhtman, Viscoelasticity and molecular rheology, in Polymer Science: A Comprehensive Reference, pp. 133–179 (Elsevier, 2012).
- R. Klajn, K.J.M. Bishop, B.A. Grzybowski, Light-controlled self-assembly of reversible and irreversible nanoparticle suprastructures. Proc. Natl. Acad. Sci. USA 104(25), 10305– 10309 (2007).
- M.A. Boles, M. Engel, D.V. Talapin, Self-assembly of colloidal nanocrystals: from intricate structures to functional materials. Chem. Rev. 116(18), 11220–11289 (2016).

Publisher's Note Springer Nature remains neutral with regard to jurisdictional claims in published maps and institutional affiliations.